Research Square

Preprints are preliminary reports that have not undergone peer review.
They should not be considered conclusive, used to inform clinical practice,
or referenced by the media as validated information.

Characterizing Severe Geomagnetic Storms and Their Magnetospheric Drivers in Solar Cycle 23 & 24

OMKAR PRASAD TRIPATHI
AKS University
PALAK SINGH THAKUR
AKS University
SWAPNIL GARG
AKS University
GAURI RICHHARIA
AKS University
SHIRSH LATA SONI
College of Liberal Arts and Sciences, 203 Van Allen Hall (VAN), Iowa City, Iowa, USA
SAKET KUMAR
saket301190@gmail.com

AKS University

Article

Keywords: Interplanetary Coronal Mass Ejections (ICMEs), Corotating Interaction Regions (CIR), Solar Activity Indicators, Interplanetary Magnetic Field (IMF), Magnetic Reconnection & Solar Wind Parameters

Posted Date: November 9th, 2026

DOI: https://doi.org/10.21203/rs.3.rs-11175193/v1

License: This work is licensed under a Creative Commons Attribution 4.0 International License.
Read Full License

Additional Declarations: No competing interests reported.

Characterizing Severe Geomagnetic Storms and Their Magnetospheric Drivers in Solar Cycle 23 & 24

OMKAR PRASAD TRIPATHI[1], PALAK SINGH THAKUR[1], SWAPNIL GARG[1], GAURI RICHHARIA[2], SHIRSH LATA SONI[3], and SAKET KUMAR[1]*

[1]Department of Physics, AKS University, Satna-485001, M.P., India
[2]Department of Electrical Engineering, AKS University, Satna-485001, M.P., India
[3]Department of Physics and Astronomy, College of Liberal Arts and Sciences, 203 Van Allen Hall (VAN), Iowa City, Iowa, USA.
Corresponding author: saket301190@gmail.com

Abstract. This study presents a systematic statistical analysis of the interplanetary drivers of severe geomagnetic storms (Dst ≤ -150 nT) over Solar Cycles 23 and 24. Utilizing OMNI plasma and magnetic field data, we investigate the relationship between storm intensity, key solar wind parameters (IMF B, Bz, Vsw, Nsw, Tsw), and solar activity proxies (SSN, F10.7). Our analysis confirms that all severe storms were unequivocally associated with prolonged intervals of southward IMF-Bz, affirming magnetic reconnection as the primary trigger mechanism. We find that the majority of events (~75%) are driven by four distinct structures: magnetic clouds (MC) and sheath fields (Sh) are the most prevalent, each responsible for 30.4% of storms, followed by combined sheath-MC structures (Sh+MC, 17.4%) and non-cloud ICMEs (17.4%). The occurrence and dominance of these drivers exhibit a strong solar cycle dependence: sheath fields and MCs prevail during the rising phase, sheath dominance peaks at solar maximum, while MCs, sheaths, and corotating interaction regions (CIRs) are the main drivers in the declining phase. Correlation analysis reveals a dominant control exerted by the peak parameters of the Interplanetary Magnetic Field (IMF), specifically the total magnetic field magnitude (B peak, CC = 0.65) and its crucial north-south component (Bz peak, CC = 0.60). These strong positive correlations highlight the direct and immediate influence of the IMF structure on storm severity. Moderate and weak relationships were observed with other solar wind parameters, including temperature (CC = -0.50) and density (CC = -0.19). Crucially, despite their fundamental role in the space environment, proxies for overall solar activity, such as the F10.7 radio flux (CC = -0.36) and sunspot number R (CC = -0.23), exhibit significantly weaker correlations with Dst peak. In stark contrast, however, geomagnetic activity indices like Kp (CC = -0.70) and Ap (CC = -0.74) show a strong negative correlation, reflecting their nature as results of the same storm phenomenon rather than its direct cause. Collectively, these findings underscore that while solar activity modulates the frequency of space weather events, the inherent physical properties of the interplanetary structures, especially the intensity and duration of southward Bz, are the most direct and potent determinants of severe geomagnetic storm intensity.

Keywords. Interplanetary Coronal Mass Ejections (ICMEs), Corotating Interaction Regions (CIR), Solar Activity Indicators, Interplanetary Magnetic Field (IMF), Magnetic Reconnection & Solar Wind Parameters.

1. Introduction

Geomagnetic storms signify one of the most intense manifestations of solar–terrestrial interactions and a major component of space weather (Gopalswamy 2022; Miteva et al. 2023; Kumar et al. 2023) arising from the efficient transfer of solar wind energy into the Earth's magnetosphere (Gopalswamy 2009; Zhang et al. 2007). These large-scale disturbances are characterized by an abrupt depression in the horizontal component of the geomagnetic field, typically quantified using the Dst and SYM-H indices (Iyemori 1990; Rostoker 1972; Nair et al. 2023; Miteva et al. 2023), which serve as direct indicators of ring current enhancement (Kumar & Verma 2023; Gonzalez et al. 1994; Iyemori 1990). The efficiency of solar wind–magnetosphere coupling depends primarily on the interplanetary magnetic field (IMF) magnitude and its sustained southward component (Bz) in Geocentric Solar Magnetospheric (GSM) coordinates, combined with high solar wind velocity (Vsw), which together govern magnetospheric energy input (Kamide et al., 1998; Tsurutani and Gonzalez, 1997).

The fundamental mechanism facilitating this coupling is magnetic reconnection at the dayside magnetopause, particularly under southward IMF conditions (Dungey, 1961; Gonzalez & Mozer, 1974; Cowley, 1982; Gonzalez et al., 1994; Cowley, 2000; Fuselier et al., 2024). This process opens previously closed magnetic flux, allowing solar wind energy and plasma to penetrate into the magnetosphere, where energy accumulates in the magnetotail and is subsequently released through substorm activity (Baker et al., 1996; Akasofu, 2017; Kumar et al., 2023). The consequential plasma injections intensify the ring current, producing the observed Dst decrease. The geomagnetic response is tracked by indices such as Kp, Ap, and the high-resolution SYM-H index, which are essential for identifying storm onset and main phase evolution (Iyemori, 1990; Rostoker, 1972; Ferradas et al., 2023; Collado-Villaverde et al., 2024).

Severe geomagnetic storms, typically defined by Dst ≤ -150 nT, are predominantly driven by transient solar phenomena, namely, Coronal Mass Ejections (CMEs) and their interplanetary manifestations (ICMEs) (Gosling, 1993; Gopalswamy et al., 2005). The ICME structure often consists of a turbulent sheath region followed by a magnetic ejecta, frequently observed as a Magnetic Cloud (MC) with enhanced magnetic field strength and smooth field rotation (Burlaga et al., 1981; Richardson and Cane, 2012; Kilpua et al., 2017). These CME-associated events are generally responsible for non-recurrent major storms, while Corotating Interaction Regions (CIRs) and High-Speed Streams (HSSs) originating from coronal holes produce moderate, recurrent storms, particularly during the declining phase of the solar cycle (Tsurutani et al., 2006; Echer et al., 2008; Kay et al., 2023; Mishra, 2024). The relative dominance of CME- and CIR-driven storms exhibits a clear solar cycle dependence (Gopalswamy, 2009; Kilpua et al., 2015; Mishra, 2024).

The present study conducts a systematic characterization of the interplanetary drivers of all severe geomagnetic storms (Dst ≤ -150 nT) during Solar Cycles 23 and 24. Using high-resolution OMNI data, we analyze solar wind parameters (B, Bz, Vsw, Nsw, Tsw), geomagnetic indices (SYM-H, Kp, Ap), and solar activity proxies (SSN, F10.7 cm flux) to: (1) identify and classify the specific interplanetary structures responsible for major storms (cf. Zhang et al., 2007; Echer et al., 2008); (2) quantify correlations between peak storm intensity and interplanetary parameters; and (3) examine solar cycle dependence of these drivers. Our findings reveal that nearly all severe storms in the 22-year interval were associated with prolonged southward IMF, with ~96% being ICME-related. We classify four dominant driver categories: (i) sheath-only events (30.4%), (ii) magnetic cloud-only events (30.4%), (iii) combined sheath MC interactions (17.4%), and (iv) non-cloud ICME ejecta (17.4%), with a minor fraction linked to CIRs. These results confirm the dominance of CME-driven storms during solar maxima and emphasize the critical role of the IMF Bz and solar wind speed in controlling storm intensity.

2. Data and Methodology

2.1 Geomagnetic Indices

To systematically analyse and track the global geo-space response to incoming space weather events, multiple geomagnetic activity indices are utilized:

Dst: The Disturbance Storm Time (Dst) index (Sugiura, 1964) serves as the primary measure of geomagnetic storm intensity in this investigation. Derived from equatorial ground-based magnetometer stations, it directly quantifies the strength of the symmetric equatorial ring current. Hourly Dst values are obtained from the World Data Center for Geomagnetism, Kyoto.

Kp: The planetary Kp index provides a 3-hour standardized indicator of geomagnetic activity and global disturbances in the Earth's magnetic field. Peak values of the Kp index are extracted during the main phase interval to gauge storm-time fluctuations.

Ap: The daily equivalent amplitude index (Ap) is incorporated on a linear scale to measure planetary geomagnetic activity. Peak Ap values are calculated during the main phase of each event to support statistical evaluations.

SYM-H: The high-resolution SYM/H index is utilized alongside Dst. Due to its 1-minute time resolution, it is essential for precisely identifying storm onset times and monitoring the fine-scale evolution of the storm's main phase.

2.2 Solar Wind and IMF Parameters

For the diagnosis of solar wind-magnetosphere coupling efficiency, in-situ interplanetary plasma and magnetic field characteristics are essential. During the storm's major phase interval, the following important hourly parameters are retrieved and evaluated for each recognized event:

B: The interplanetary magnetic field's overall strength (IMFB).

Bz: The important north-south component of the IMF in Geocentric Solar Magnetospheric (GSM) coordinates (IMF Bz), where magnetic reconnection at the dayside magnetopause is governed by persistent negative values ($Bz < 0$).

Vsw: The bulk velocity or velocity magnitude of the solar wind (Vsw).

Nsw: The density of protons in the solar wind.

Tsw: The temperature of the solar wind plasma.

2.2.1 ACE and OMNI Sources

The interplanetary data utilized in this analysis are compiled from two complementary sources:

Advanced Composition Explorer (ACE): We used high-resolution (usually 16-second or 64-second) plasma and magnetic field data from the Solar Wind Electron, Proton, and Alpha Monitor (SWEPAM) and Magnetometer (MAG) instruments on board the ACE spacecraft to precisely identify the interplanetary structures (e.g., shock sheaths, magnetic clouds) responsible for storm commencement (Stone et al., 1998). An energetic 30-to-60-minute advance warning of approaching helio-spheric structures is provided by ACE, which is positioned at the L_1 Lagrangian point (~1.5 million km upstream of Earth).

OMNI Hourly Data: We used hourly data from the OMNIWeb database in order to do a methodical statistical study of storm parameters. The Dst index, solar wind speed (Vsw), solar wind temperature (Tsw), solar wind density (Nsw), the magnitude of the interplanetary magnetic field (IMF B), its southward component in GSM coordinates (IMF Bz), the planetary K-index (Kp), the daily sunspot number (R), the equivalent daily Ap index, and the F10.7 cm solar radio flux are all included in Table 1. Each geomagnetic storm's main phase, according to Gonzalez et al. (1994), is the time between the Dst index's beginning rapid decrease and its peak negative value. Peak IMF B, peak negative IMF Bz, peak Vsw, peak Tsw, peak Nsw, peak Kp, peak R, peak Ap, and peak F10.7 flux were all measured for each event during the main phase.

2.3 Solar Activity Parameters

To quantify and differentiate long-term solar cycle variations and ambient background levels from short-term eruptive phenomena, specific solar proxies are monitored:

Sunspot Number (SSN): As a traditional proxy for monitoring the general appearance of magnetic flux and active areas on the solar disk, the daily sunspot number (R) is gathered.

F10.7 Flux: A reliable indicator of solar extreme ultraviolet (EUV) and X-ray emission activity, the daily F (10.7) solar radio flux tracks variations in the solar corona and upper chromosphere.

2.4 Solar Eruptive Events

The solar origins and preliminary triggers of severe geomagnetic activity are established using correlative space-based remote sensing observations:

CMEs (LASCO): The Solar and Helio-spheric Observatory (SOHO) spacecraft's Large Angle and

Spectrometric Coronagraph (LASCO) (Brueckner et al., 1995) and Extreme Ultraviolet Imaging Telescope (EIT) (Delaboudinière et al., 1995) provide white-light observations of Coronal Mass Ejections (CMEs). Important geometric and dynamic characteristics, such as the time of initial appearance, angular breadth, center position angle, and linear speed, are obtained from LASCO data, allowing for direct correlations between downstream ICMEs seen at ACE and Earth-directed eruptions, such as halo CMEs (Webb & Howard, 2012). Similar solar surface activity, such as dimming areas or post-eruption arcades, which are indicators of a CME's source location, were found using EIT data.

Solar Flares (GOES): The National Centers for Environmental Information (NCEI) STP solar data site and the Space Weather Prediction Center (SWPC) solar event reports are used to derive the time, duration, and energy characteristics of flare occurrences. The Geostationary Operational Environmental Satellites (GOES) classify flares into A, B, C, M, and X classes according to their peak soft X-ray flux; each class denotes a ten-fold increase in intensity (e.g., Garcia, 1994) to determine the total eruptive magnitude of the source active regions.

2.5 Data Collection Pipeline

The empirical database compiled for this study was built by systematically gathering space-based and ground-based observations from several open-access space weather repositories. The data collection architecture is divided into three primary segments:

Geomagnetic Index Retrieval: The World Data Center (WDC) for Geomagnetism at Kyoto University in Japan provided continuous high-resolution hourly time-series data for the Dst and SYM/H indices. These statistics offer the fundamental baseline needed to determine storm timeframes and measure the severity of ring currents.

Interplanetary and Ambient Solar Wind Data: The NASA OMNI Web data explorer was used to gather interplanetary magnetic field vectors (B, Bz) and in-situ solar wind plasma characteristics (Vsw, Tsw, Nsw, Kp, Ap, SSN, SRF). Time-shifted, cross-calibrated observations from many helio-spheric satellites are combined in this database. Raw high-resolution images were obtained straight from the Advanced Composition Explorer (ACE) Science Center for fine-scale structural identification of shocks, sheaths, and ejecta boundary layers.

2.6 Event Selection and Analysis Procedure

The event selection is governed by a strict threshold-driven pipeline to guarantee a focused analysis on severe geomagnetic storm events:

Selection Threshold: During Solar Cycles 23 (1996–2006) and 24 (2008–2018), 29 significant geomagnetic storms with a minimum $Dst \leq -150\, nT$ are found and examined. According to Tsurutani et al. (2006) & Kumar et al. (2026) this criterion is chosen to concentrate on extreme, geoeffective occurrences with a high potential for technological repercussions.

Phase Identification: According to Gonzalez et al. (1994), the major phase of each individual geomagnetic storm was defined as the time period between the Dst index's first abrupt drop or decline and its greatest negative peak value (Dst).

Main Phase Parameter Extraction: The peak conditions of the driving interplanetary medium and corresponding solar characteristics were identified within this precise main phase window for every solitary storm interval. Peak values for peak IMF B, peak negative IMF Bz, peak Vsw, peak Tsw, peak Nsw, peak Kp, peak SSN (R), peak Ap, and peak F (10.7) flux are all collected.

Statistical and Structural Association: In order to map the whole physics from solar origin to terrestrial destination, the combined dataset is methodically cross-correlated to categorize the causal interplanetary configurations (such as pure shock sheaths, magnetic clouds, and composite structures) against solar eruptive inputs. Table 1 displays the data that was analyzed:

Table 1. Interplanetary Structure That Causes Severe Geomagnetic Storm during Solar Cycles 23 and 24 (Chi et. al., 2016; Richardson and Cane, 2012, Kumar et. al., 2026).

Year	On set time day(hour)	Date	Peak Dst (nT)	IP Structure	Type of CME	Type of Flares
1998	124(5)	5/4/1998	-205	SH	Halo CME	X-class SF
1998	239(9)	8/27/1998	-155	non-MC	Halo CME	X-class SF
1998	268(9)	9/25/1998	-207	SH	No data	no data
1999	265(23)	9/22/1999	-173	sMC	Partial Halo	X-class SF
1999	295(06)	10/22/1999	-237	non-MC/CIR	Halo CME	X-class SF
2000	98(0)	4/7/2000	-292	SH	Halo CME	M-Class SF
2000	198(0)	7/16/2000	-300	sMC	Halo CME	X-class SF
2000	225(9)	8/12/2000	-234	nonMC	Halo CME	C-class SF
2000	261(23)	9/17/2000	-201	SH/MC	Halo CME	C-class SF
2000	279(13)	10/5/2000	-181	MC	Halo CME	M-class SF
2000	311(21)	11/6/2000	-159	COMPLEX	Halo CME	C-class SF
2001	90(8)	3/31/2001	-387	SH/MC	Halo CME	X-class SF
2001	101(23)	4/11/2001	-271	SH/MC	Halo CME	M-class SF
2001	276(14)	10/3/2001	-166	sMC	Halo CME	X-class SF
2001	294(23)	10/21/2001	-187	SH	Halo CME	X-class SF
2001	301(11)	10/28/2001	-157	SH	Halo CME	X-class SF
2001	328(16)	11/24/2001	-221	SH/MC	Halo CME	X-class SF
2002	251(0)	9/8/2002	-198	SH/non-MC	Halo CME	X-class SF
2002	274(16)	10/1/2002	-176	sMC	Halo CME	M-Class SF
2003	303(22)	10/30/2003	-480	SH/MC	Halo CME	X-class SF
2003	324(21)	11/20/2003	-422	SH	Partial Halo	M-Class SF
2004	313(6)	11/8/2004	-374	sMC	Halo CME	C-class SF
2005	135(8)	5/15/2005	-320	sMC	Halo CME	X-class SF
2005	236(11)	8/24/2005	-184	SH/MC	Halo CME	M-Class SF
2006	349(5)	12/15/2006	-224	sMC	Halo CME	X-class SF
2015	76(22)	3/17/2015	-234	SH/CIR	Halo CME	M-Class SF
2015	174(4)	6/23/2015	-198	SH/MC	Halo CME	M-Class SF
2015	354(22)	12/20/2015	-166	sMC	Halo CME	B-class SF
2018	238(7)	8/26/2018	-176	SH/MC	Partial Halo	B-class SF

CIR = Corotating Interaction Region, **MC =** ICME that shows the signature of a typical magnetic cloud, **SMC =** Magnetic cloud preceded by fast shock, SH = Sheath Field, **SH/MC =** Sheath Field followed by a magnetic cloud, non-MC = ICME that doesn't show the signature of a magnetic cloud, **SH/non-MC** = ICME without magnetic cloud (non-MC), COMPLEX = Presence of shock–shock, shock–CME, or CME–CME interactions, **SH/CIR =** A shock associated with or driven by a Corotating Interaction Region. In this study, the term "small magnetic cloud" (sMC) refers to structures with durations substantially shorter than the canonical MC duration of ~20–30 h, typically lasting less than 12 h. Despite their shorter duration, these structures retain explicit flux-rope signatures, such as smooth magnetic field rotation, enhanced magnetic field strength, and low proton temperature (Richardson & Cane, 2012; Kilpua et al., 2017, Kumar et. al., 2026).

3. Result and Discussion

In the present study, the interplanetary structure and corresponding geomagnetic signatures of Interplanetary Coronal Mass Ejections (ICMEs) have been analyzed to understand their propagation characteristics and geo-effectiveness. As illustrated in figure 1(*Richarson & Cane, 2012; Thakur et. al, 2025, Kumar et.al., 2026*, the ICME originates from the Sun and expands outward through the heliosphere. Due to its high propagation velocity relative to the ambient solar wind, a shock front develops ahead of the ICME. Immediately behind this shock lies a turbulent sheath region, characterized by compressed plasma and fluctuating

magnetic fields, followed by the magnetic cloud, which represents the core of the ICME. The magnetic cloud typically exhibits a smoothly rotating magnetic field, low plasma beta, and enhanced magnetic field strength, indicative of a flux-rope structure. The presence of counter streaming electrons and enhanced electron heat flux further confirms the closed magnetic topology of the ICME.

Panels (A) and (B) of figure 1 show the geomagnetic response associated with these interplanetary structures. In the first case (panel A), where an ICME with a strong southward interplanetary magnetic field (IMF Bz < 0) encounters Earth's magnetosphere, significant magnetic reconnection occurs, leading to a pronounced geomagnetic storm. The arrival of the shock (S) produces a sudden increase in solar wind speed and dynamic pressure, corresponding to a sudden storm commencement (SSC). The subsequent sheath region, with its turbulent and variable magnetic field, and the magnetic cloud, with its prolonged southward IMF orientation, together drive the main phase of the storm, reflected as a marked decrease in the Dst index due to enhanced ring current activity. As the IMF turns northward, the recovery phase begins, and the Dst gradually returns toward quiet levels. This sequence defines the typical storm evolution through distinct phases-sudden commencement, main phase, and recovery phase.

In contrast, panel (B) illustrates an event where only a shock or weak ICME passage occurs, producing a sudden positive impulse in the Dst index at shock arrival without a significant southward IMF component thereafter. Such events are non-geoeffective and result only in an SSC, without the development of a main phase depression. This comparative analysis highlights that the southward IMF orientation within the sheath or magnetic cloud is the primary driver of intense geomagnetic storms, whereas shock-only or weak ICME events contribute minimally to geomagnetic disturbances.

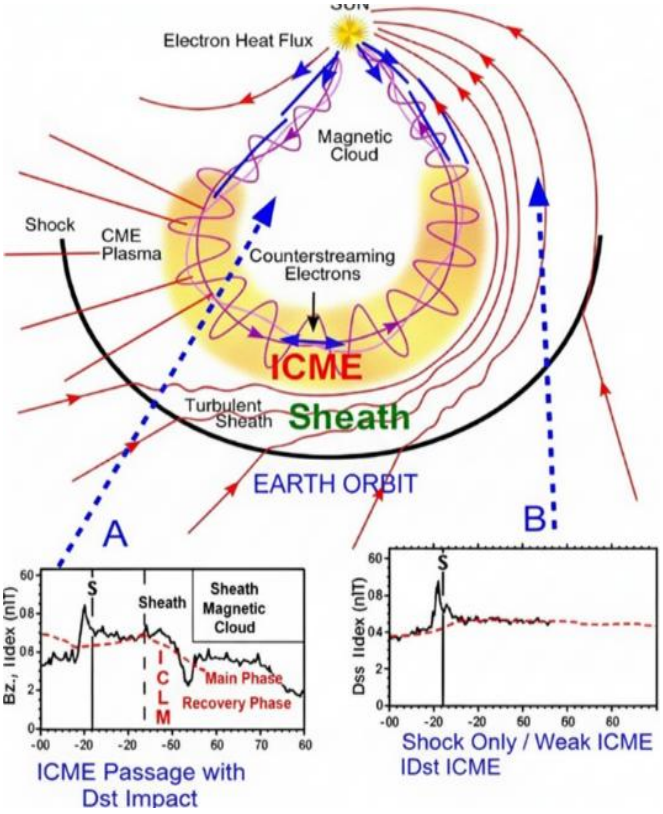


Figure 1: Schematic of an interplanetary coronal mass ejection driving a shock ahead of it and the associated variations in the galactic cosmic ray intensity along trajectories that do (A) or do not (B) encounter the ICME. (Richarson & Cane, 2012; Thakur et. al, 2025, Kumar et.al., 2026)

3.1 Occurrence and Solar Cycle Dependence of Severe Storms

The frequency, severity, and solar eruptive origins of the 29 severe geomagnetic storms (Dst ≤ −150 nT) observed over the 22-year period from 1996 to 2019 reveal a pronounced asymmetry between Solar Cycle (SC) 23 and SC 24. These differences are evident in the storm occurrence rate, intensity, and associated solar eruptive drivers, as summarized in Table 1. Of the 29 severe geomagnetic storms, only four events (≈14%) occurred during SC 24, whereas 25 events (≈86%) were recorded during SC 23. SC 23 exhibited a prolonged period of high geomagnetic activity, particularly during its active phase in 2000–2002, with an annual occurrence rate of up to six severe storms (Figure 2). In contrast, SC 24 was characterized by substantially reduced geomagnetic activity, with three severe storms occurring around its peak in 2015 and only one event during its declining phase. The occurrence of a severe storm during the declining phase of SC 24

represents a relatively unusual feature of the cycle. This marked reduction in severe-storm occurrence reflects the comparatively weak solar activity and reduced solar-wind energy input during SC 24, which is recognized as one of the weakest solar cycles of the last century. Figure 2 illustrates the annual distribution of severe geomagnetic storms during SC 23 and SC 24, highlighting the pronounced contrast in geomagnetic activity between the two cycles.

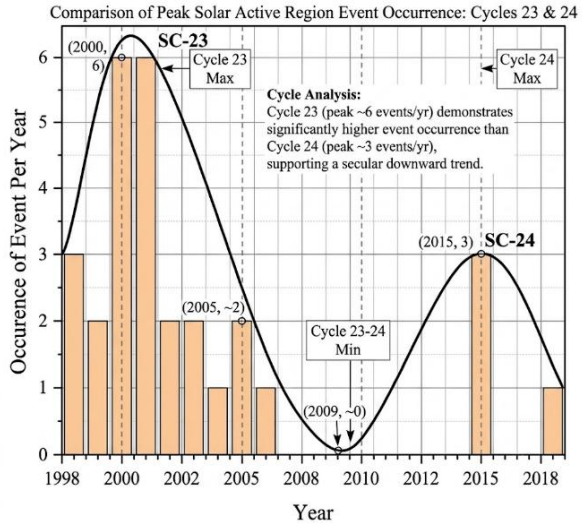


Figure 2: Histogram showing the yearly occurrence of severe geomagnetic storms during Solar Cycles 23 and 24. The figure illustrates temporal variability in storm frequency, highlighting years with enhanced geomagnetic activity across the two cycles.

Solar Flare Association: Only one of the 29 severe storms had complete data missing, whereas 28 incidents (96.6%) were associated to solar flares of different kinds. Figure 4 illustrates that very powerful X-class solar flares drove 50% (14 out of 28) of these storms, whereas M-class flares were responsible for 28.6% (8 out of 28). The little remaining proportion was made up of B-class (7.1%) and C-class (14.3%) flares. The sample is dominated by X-class flares, although CME geo-effectiveness cannot be determined only by flare amplitude. Prior studies have shown that source-region magnetic configuration, flux-rope structure, and CME kinematics are equally important (e.g., Kawabata et al., 2018). As a result, the high frequency of X- and M-class eruptions in this dataset emphasizes that, even the energetic solar active regions are very good at producing severe events, in order to properly evaluate the ultimate geo-space impacts, they must be examined in conjunction with the physical evolution of the related interplanetary structure. Figure 3 shows the distribution of flare classes linked to the detected storm-producing events.

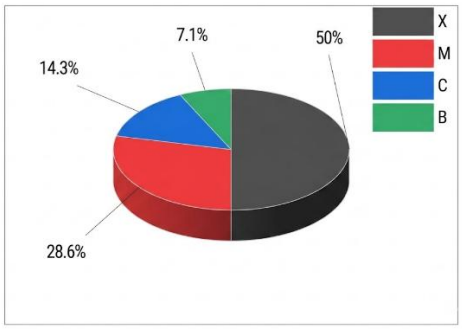


Figure 3: Classification of solar flares into different categories based on their X-ray intensity. The figure presents the distribution of flare types, highlighting the relative occurrence of B-, C-, M-, and X-class flares within the dataset.

CME Association: The spatial morphology of the driving CMEs exhibits a distinct preference for Earth-directed trajectories. Among the flare-associated events, 89.3% (25 out of 28) were classified as full Halo CMEs, exhibiting a complete 360∘ brightening around the coronagraph occulting disk (Figure 4). Recent studies have shown that the occurrence rate of Halo CMEs normalized to sunspot number was higher during SC24 and SC25 than during SC23 (Gopalswamy et al., 2023). Therefore, the high Halo-CME fraction observed in our storm-producing sample should not be interpreted solely as a consequence of stronger solar activity, but rather as evidence that Earth-directed CME geometry remains a key factor in determining geomagnetic effectiveness. The remaining 10.7% (3 out of 28) were Partial Halo CMEs with angular widths spanning 120º to 360º. The overwhelming prevalence of Halo CMEs demonstrates that severe geomagnetic storms require central, Earth-directed eruptive configurations to maximize helio-spheric geo-effectiveness. This trend aligns with earlier findings (Gopalswamy et al., 2009; Zhang et al., 2007), reinforcing the notion that energetic solar flare-CME systems play a crucial role in driving major geomagnetic disturbances. Such results provide a valuable framework for forecasting CME geo-effectiveness in Solar Cycle 25, particularly as more sophisticated coronagraph observations from missions like SOHO, STEREO, and the upcoming Solar Orbiter enhance our capability to monitor and predict Earth-directed solar eruptions. The distribution of CME classes associated with the

identified storm-producing events is illustrated in Figure 4.

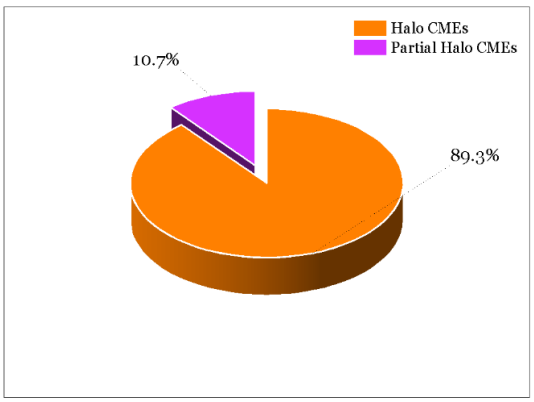


Figure 4: Classification of coronal mass ejections (CMEs) based on their observed characteristics. The figure illustrates the distribution of different CME types, including halo, partial halo, and other categories, as identified in the dataset.

By contrasting specific severe occurrences, this solar cycle reliance is further supported. During SC-23 compared to SC-24, there were significantly more severe storms that met the selection criterion (Dst < -150 nT). However, quantitative comparisons between the two cycles should be regarded cautiously because just four occurrences were found during SC-24. While relatively weaker peak events were recorded during SC-24 (e.g., March 2015 with Dst = -234 nT) and landmark, ultra-severe storms occurred during SC-23 (e.g., October 2003 'Halloween Storms' with Dst = -480 nT), the stark asymmetry in sample size (25 events vs. 4 events) prevents treating the two cycles as statistical equals for cycle-to-cycle comparisons. Figure 5 shows representative storm episodes and the interplanetary structures that are connected to them.

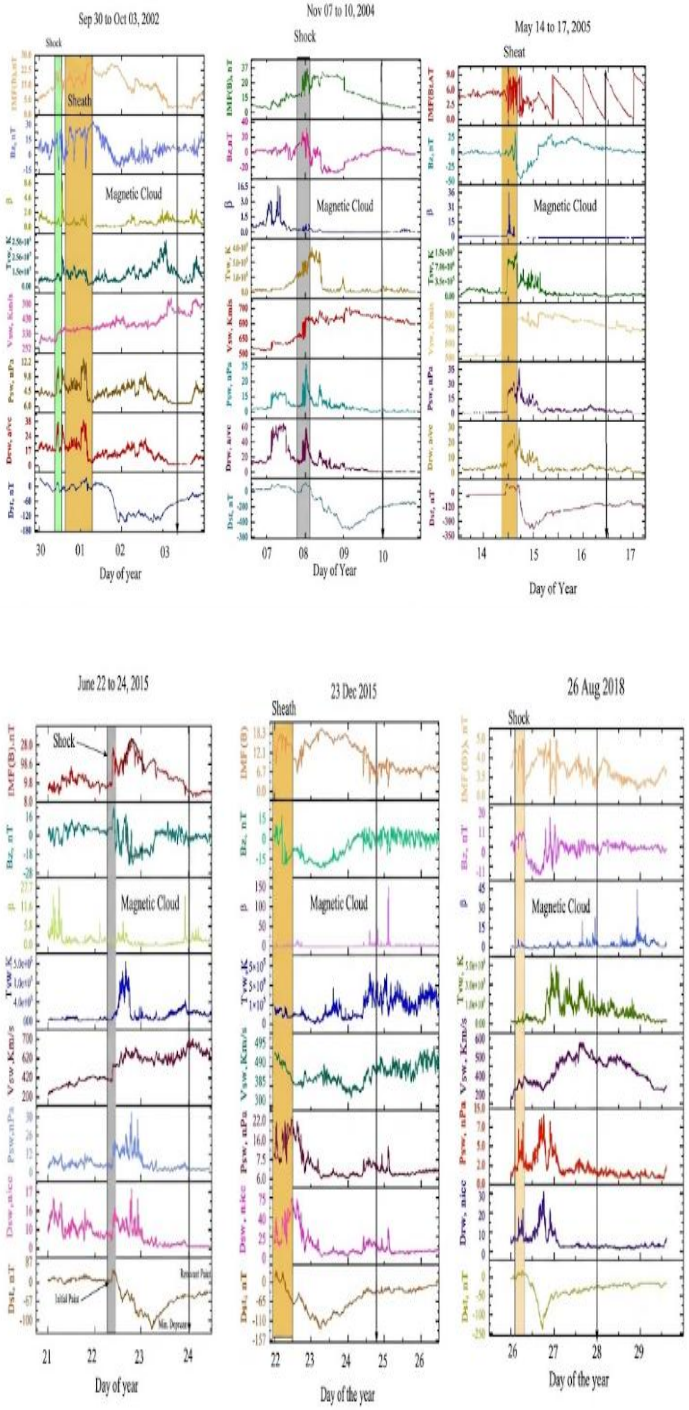


Figure 5: Selected sever geomagnetic storm events and their associated interplanetary structures during Solar Cycles 23 and 24. The figure highlights representative events illustrating the interplanetary drivers such as ICMEs, magnetic clouds, and CIRs that were responsible for generating intense geomagnetic disturbances throughout the two cycles.

3.2 Interplanetary Drivers of Severe Storms

To determine the precise helio-spheric structures responsible for triggering these 29 severe events, a comprehensive comparative analysis of transient interplanetary (IP) configurations was performed. The statistical distribution reveals that interplanetary coronal mass ejection (ICME)-driven structures, rather than corotating interaction regions (CIRs), are the primary agents of extreme geo-space disturbances. Small magnetic clouds (sMC) preceded by fast shocks and combined shock–magnetic cloud (SH/MC) structures represent the most efficient configurations for energy transfer, each accounting for 8 events (28.6%, for a collective total of 57.2%). Pure shock-associated sheath (SH) fields were responsible for 6 events (21.4%), whereas non-magnetic cloud (non-MC) ICME ejecta structures were relatively rare, occurring in only 2 cases (7.1%). Mixed or complex configurations, including non-MC/CIR interactions, SH/non-MC structures, pure magnetic clouds (MC), and complex shock–shock/CME–CME multi-ejecta intervals, each accounted for a minor fraction of 3.6% (Figure 6).

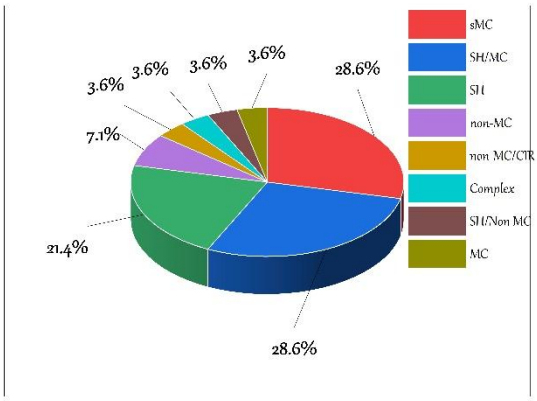


Figure 6: Comprehensive comparative analysis of interplanetary (IP) structures associated with major geomagnetic storm events during Solar Cycles 23 and 24. The figure contrasts the dominant storm-driving mechanisms such as ICMEs, magnetic clouds, and CIRs highlighting their relative occurrence and characteristics across the two solar cycles.

The internal magnetic field structure of sMCs and SH/MC drivers is directly responsible for their unique effectiveness. In addition to a smooth, extended rotation of the southbound IMF component ($Bz < 0$) and a high solar wind velocity, these structures usually exhibit an increased total magnetic field strength. Massive plasma injections into the equatorial ring current are caused by these circumstances, which maintain high rates of magnetic reconnection near Earth's dayside magnetopause. Sheath-only (SH) fields may cause strong, instantaneous geomagnetic depressions while lacking the organized flux-rope structure of magnetic clouds due to their extremely compressed, turbulent, and fluctuating magnetic fields. On the other hand, it is demonstrated that pure CIR structures or high-speed streams without ICME interactions are extremely inefficient at producing severe storms ($Dst \leq -150nT$), indicating that transient solar eruptive structures, rather than recurrent streams, are nearly exclusively responsible for extreme space weather events.

3.3 Correlation Analysis

To quantify the direct physical control exerted by the interplanetary medium over geomagnetic storm intensity, a detailed statistical correlation analysis was executed between the peak negative Dst (Dst peak) and key interplanetary parameters, geomagnetic indices, and solar proxies:

Interplanetary Magnetic Field Control: The correlation coefficient (CC) evaluations demonstrate that the magnetic configuration of the incoming structure is the absolute mathematical determinant of storm severity. The peak total magnetic field magnitude (Bpeak) shows a strong positive correlation of $CC = 0.65$(Figure 7b), while the peak southward component (Bzpeak) exhibits a critical correlation of $CC = 0.60$ (Figure 7a). These values mathematically validate that the immediate magnitude of the geomagnetic ring current depression is fundamentally dictated by the amplitude and orientation of the IMF vector driving the dayside reconnection rate.

Solar Wind Thermal and Plasma Parameters: Moderate to weak relationships were observed among the kinetic properties of the solar wind. Solar wind plasma temperature (Tsw) displays a moderate correlation of $CC = -0.50$ (Figure 7c), highlighting the role of thermal expansion and compression across shock structures. In contrast, solar wind proton density (Np) exhibits a highly scattered, weak correlation of $CC = -0.19$ (Figure 7d), confirming that density alone does not dictate ultimate storm severity.

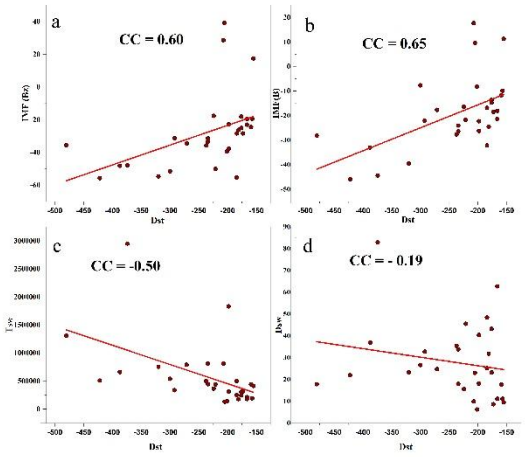


Figure 7: Scatter plots showing the relationship between peak Dst and key solar wind parameters. The figure presents correlations between peak Dst and (a) total IMF magnitude (B), (b) southward IMF component (Bz), (c) solar wind temperature, and (d) solar wind density, illustrating how variations in interplanetary conditions influence geomagnetic storm intensity.

Geomagnetic Activity Indices Comparison: A stark, highly significant negative correlation was verified between Dst peak and global geomagnetic indices, with the Ap index yielding $CC = -0.74$ (Figure 8c) and the Kp index yielding $CC = -0.70$ (Figure 8a). It must be emphasized that these high correlation coefficients reflect the fact that Kp, Ap, and Dst are simultaneous mathematical consequences of the same global magnetospheric storm phenomenon, rather than a cause-and-effect relationship.

Solar Activity Proxies: Crucially, long-term proxies for baseline solar activity exhibit the weakest correlation to individual storm intensity. The F10.7 solar radio flux shows a weak correlation of $CC = -0.36$(Figure 8d), while the daily Sunspot Number (R) drops to an extremely weak $CC = -0.23$ (Figure 8b). Although F (10.7) radio flux and sunspot number are not direct drivers of geomagnetic storms, they are widely used proxies of overall solar magnetic activity. Previous studies have reported that storm occurrence rates vary with solar cycle activity; therefore, these parameters were included to examine whether storm intensity itself exhibits any dependence on long-term solar activity levels. The weak correlations obtained here indicate that while solar activity modulates the probability of CME occurrence, the intensity of an individual geomagnetic storm is primarily controlled by the local interplanetary conditions, particularly the magnitude and duration of southward IMF Bz. This mathematical decoupling demonstrates a vital physical truth: while long-term solar activity cycle factors modulate the *frequency* and *probability* of active region generation, they exert virtually no direct control over the ultimate *intensity* of an individual severe storm. The severity of a specific space weather event is solely governed by the localized, internal physical properties of the striking interplanetary structure specifically the magnitude and duration of the southward IMF Bz.

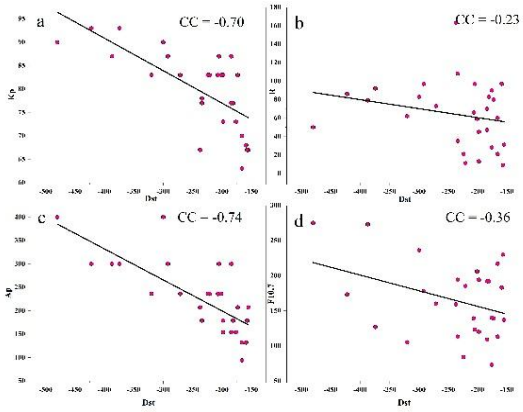


Figure 8: Scatter plots illustrating the relationship between peak Dst and key solar activity indices and proxies. The figure shows correlations between peak Dst and (a) Ap index, (b) Kp index, (c) F10.7 solar radio flux, and (d) sunspot number (R), highlighting how variations in solar activity and long-term solar proxies relate to geomagnetic storm intensity.

3.4 Comparison with Previous Studies

Our statistical analysis of 29 severe geomagnetic storms shows excellent alignment with key long-term space weather surveys. Our results confirm the findings of Gopalswamy et al. (2015), demonstrating that magnetic clouds and compressed shock sheaths remain highly geoeffective despite the diminished helio-spheric pressure of Solar Cycle 24 (SC24). The severe storm asymmetry between the two cycles where ~86% of events occurred during SC23 directly reflects the physical mechanisms identified by Shi et al. (2024). Their work showed a systematic weakening of the near-Earth solar wind and ambient pressure during SC24, which allowed traveling CMEs to undergo

anomalous volume expansion. This expansion diluted their internal magnetic field strengths, resulting in weaker southward IMF Bz components at 1 AU and leading to the lower frequency of severe storms observed in our SC24 dataset. Additionally, the overwhelming dominance of CME-driven structures (~96%) identified in this study agrees with the statistical frameworks of Reyes et al. (2021) and Sandeep Kumar et al. (2024). These authors emphasized that while long-term solar activity proxies (SSN and F (10.7) modulate event frequency, they decouple from individual storm intensity. Instead, as verified by our strong correlations with (B peak, $CC = 0.65$) and (Bz peak, $CC = 0.60$), the ultimate severity of a space weather event is dictated by the localized, internal structural properties of the incoming driver rather than ambient solar cycle strength.

3.5 Solar Wind Dynamic Pressure and Ambient Helio-spheric Conditions

To investigate the broader helio-spheric conditions that may have contributed to the contrasting storm intensities between Solar Cycles 23 and 24, we examined the solar-wind dynamic pressure (Pdyn). Our analysis reveals a pronounced reduction in both the background and peak (Pdyn) during SC24 compared with SC23, indicating a substantially weaker helio-spheric environment. Previous studies have reported a similar reduction in the ambient solar-wind total pressure during SC24, with the average total pressure at 1 AU decreasing by approximately 30% relative to SC23 (Gopalswamy et al., 2015). This weakened helio-spheric pressure environment has been linked to anomalous expansion of CMEs during their propagation, particularly in the inner heliosphere, which can dilute their magnetic content and consequently reduce the magnetic-field strength carried by ICMEs to 1 AU (Gopalswamy et al., 2014; Gopalswamy et al., 2015). The reduced magnetic content and weaker CME fields in SC24 are consistent with the substantially lower geo-effectiveness of magnetic clouds, including weaker (VxBz) and less intense Dst responses, compared with SC23 (Gopalswamy et al., 2015). More recent statistical analysis further indicates that, despite the lower ambient pressure, the average radial sizes of ICMEs and magnetic clouds at 1 AU were actually smaller in SC24, suggesting that the reduced helio-spheric pressure was largely compensated by a reduction in the magnetic content and internal pressure of CMEs (Gopalswamy et al., 2021). Therefore, the reduced (Pdyn) in SC24 should be viewed not simply as a direct cause of larger ICMEs at 1 AU, but as an important component of a coupled helio-spheric process involving weaker CME magnetic content, anomalous expansion, and reduced magnetic-field strength. These conditions ultimately limited the magnitude and duration of southward IMF (Bz), weakened solar-wind–magnetosphere coupling, and contributed to the substantially lower occurrence and intensity of severe geomagnetic storms during SC24 compared with SC23.

4. Conclusion

Using OMNI solar-wind and interplanetary magnetic-field measurements, this work offers a comprehensive statistical evaluation of the interplanetary causes and solar-cycle dependency of severe geomagnetic storms $Dst \leq -150\ nT$ during Solar Cycles 23 and 24. The findings confirm magnetic reconnection as the primary mechanism for transferring solar-wind energy into the terrestrial magnetosphere and show that the magnitude, orientation, and persistence of the southward IMF component (Bz) determine the geo-effectiveness of an interplanetary structure. Peak IMF magnitude (Bpeak), $CC = 0.65$, and peak southbound IMF component (Bzpeak), $CC = 0.60$, showed the highest correlations with storm severity, whereas solar-wind density and solar-activity proxies like sunspot number and F10.7 showed much smaller correlations.

The categorization of interplanetary drivers reveals that, at around 30.4% each, magnetic clouds (MCs) and sheath areas are the main causes of severe geomagnetic storms, followed by non-cloud ICMEs and combination sheath–MC structures. In general, CIRs contribute relatively little to catastrophic occurrences, but CME-related structures account for the vast bulk of them. The distribution of these drivers also shows a dependency on the solar cycle phase, with MCs, sheaths, and CIRs contributing during the decreasing phase and sheath and MC structures being especially significant during the rising and maximum phases. This phase-dependent trend highlights how solar-cycle activity affects both the relative occurrence of various geoeffective structures and the frequency of interplanetary disruptions. A pronounced contrast is also observed between Solar Cycles 23 and 24. SC23 produced the

majority of severe storms identified in the present dataset, whereas SC24 exhibited a substantially lower occurrence rate and weaker geomagnetic activity. This cycle-to-cycle difference is consistent with the weaker solar-wind and helio-spheric conditions characteristic of SC24, including reduced solar-wind dynamic pressure and weaker magnetic-field conditions. Such background helio-spheric conditions can influence CME expansion and magnetic-field dilution during propagation, thereby reducing the geo-effectiveness of ICMEs arriving at Earth. Thus, the lower occurrence of severe storms during SC24 cannot be attributed solely to a reduced number of solar eruptions; it also reflects changes in the interplanetary environment and the magnetic properties of the structures interacting with the Earth's magnetosphere.

An important outcome of this study is that the occurrence rate of geomagnetic storms and their eventual intensity should be considered as two related but physically different quantities. Solar activity proxies such as SSN and F10.7 provide information about the overall level of solar activity and may help characterize the probability of eruptive events, but they do not directly determine the intensity of an individual geomagnetic storm. Once an interplanetary disturbance reaches 1 AU, its magnetic-field strength, particularly the magnitude and duration of southward (Bz), together with its solar-wind velocity and associated dynamic pressure, becomes much more important for determining the resulting geomagnetic response. Consequently, space-weather prediction models should place greater emphasis on the in-situ characterization of CME sheaths, magnetic clouds, and other ICME structures rather than relying solely on solar activity indices.

The findings also provide a useful observational framework for interpreting the evolving activity of Solar Cycle 25. However, the relatively small number of severe storms identified during SC24 limits the statistical robustness of direct cycle-to-cycle comparisons. Although the pronounced asymmetry between SC23 and SC24 is evident, conclusions concerning long-term changes in the occurrence and physical properties of severe geomagnetic storms should therefore be regarded as indicative rather than definitive. Extending the present analysis to include the complete Solar Cycle 25, together with larger event samples and additional parameters such as the minimum (Bz), duration and integrated southward (Bz), (V x Bz), solar-wind dynamic pressure, CME propagation characteristics, and CME–CME interaction signatures, will provide stronger constraints on the physical mechanisms controlling extreme geomagnetic activity.

Overall, the present results demonstrate that severe geomagnetic storms are controlled primarily by the magnetic and plasma characteristics of the interplanetary structures that reach Earth, rather than by the magnitude of the solar cycle alone. The identification and timely characterization of strongly southward magnetic fields within CME sheaths and magnetic clouds therefore remain essential for improving the prediction of severe geomagnetic storms and strengthening operational space-weather forecasting capabilities.

Acknowledgements: The authors are grateful to the NASA OMNI Web service and the Space Physics Data Facility (SPDF) for providing cross-calibrated interplanetary solar wind and IMF data and to the Advanced Composition Explorer (ACE) Science Center for high-resolution in situ observations. We acknowledge the World Data Center (WDC) for Geomagnetism at Kyoto University, Japan, for the Dst and SYM-H indices used to identify geomagnetic storm timelines. We also thank the SOHO/LASCO and EIT teams for the CME coronagraph data and the NOAA Space Weather Prediction Center (SWPC) along with NCEI for the solar flare X-ray event reports.

Data Availability: The datasets analyzed in this study are publicly available from established scientific data repositories. Solar-wind plasma parameters and interplanetary magnetic field (IMF) data were obtained from the NASA Space Physics Data Facility (SPDF) OMNIWeb service (https://omniweb.gsfc.nasa.gov/form/dx1.html) and its high-resolution data interface (https://omniweb.gsfc.nasa.gov/form/omni_min.html). Geomagnetic indices, including the disturbance storm time (Dst) index, were obtained from the World Data Center for Geomagnetism, Kyoto (https://wdc.kugi.kyoto-u.ac.jp/). Additional solar-wind observations, where applicable, were obtained from the Advanced Composition Explorer (ACE) Science Center (https://izw1.caltech.edu/ACE/ASC/). Coronal mass ejection (CME) parameters from

SOHO/LASCO observations were obtained from the NASA CDAW SOHO/LASCO CME Catalog (https://cdaw.gsfc.nasa.gov/CME_list/index.html). Relevant solar and space-weather data were obtained from the NOAA Space Weather Prediction Center (https://www.swpc.noaa.gov/). These repositories provide public access to the observational datasets and associated documentation used in this study.

Declaration of AI Use: - The authors used Grammarly and ChatGPT for grammar checking, language refinement, and reference formatting. These tools were not assigned authorship and did not replace the authors' scientific judgement. All AI-assisted outputs were reviewed and verified by the authors, who accept responsibility for the accuracy, integrity, and final content of the manuscript.

Conflict of Interests: - We, the authors, confirm that we have no conflict of interest related to this research.

Funding: No, this research did not receive funding.

References

Akasofu S.-I. 2017, Exploring the Secrets of the Aurora, Springer, Tokyo.

Baker D. N., Pulkkinen T. I., Angelopoulos V., Baumjohann W., McPherron R. L. 1996, J. Geophys. Res., 101, 12975.

Burlaga L. F., Sittler E., Mariani F., Schwenn R. 1981, J. Geophys. Res., 86, 6673.

Chi Y., et al. 2016, Solar Physics, 291, p.2419.

Cowley S. W. H. 1982, Rev. Geophys., 20, 531.

Cowley S. W. H. 2000, Ann. Geophys., 18, 1004.

Collado-Villaverde A., et al. 2024, Nat. Hazards (in press).

Dungey J. W. 1961, Phys. Rev. Lett., 6, 47.

Echer E., Gonzalez W. D., Tsurutani B. T., Gonzalez A. L. C. 2008, J. Geophys. Res., 113, A05221.

Ferradas C. P., Fok M.-C., Maruyama N., et al. 2023, Front. Astron. Space Sci., 10, 1278820.

Fuselier S. A., et al. 2024, Space Sci. Rev. (in press).

Gopalswamy N. 2009, in *Aeronomy of the Earth's Atmosphere and Ionosphere*, eds. Tsuda T., Fujii R., Shibata K., Geller M. A., Springer, Dordrecht.

Gopalswamy N., Yashiro S., Liu Y., Michalek G., Vourlidas A., Kaiser M. L., Howard R. A. 2005, J. Geophys. Res., 110, A09S15.

Gopalswamy N. 2022, arXiv:2211.06775.

Gopalswamy et al. 2023, ApJ, 952, p.13.

Gopalswamy, N., et al. (2021). *Frontiers in Astronomy and Space Sciences, 8*, 713999.

Gopalswamy N., Tsurutani B. T., & Yan Y. 2015. Journal of Geophys. Research: Space Phys., 120, p.9231.

Gonzalez W. D., Mozer F. S. 1974, J. Geophys. Res., 79, 4186.

Gonzalez W. D., Joselyn J. A., Kamide Y., Kroehl H. W., Rostoker G., Tsurutani B. T., Vasyliunas V. M. 1994, J. Geophys. Res., 99, 5771.

Gosling J. T. 1993, J. Geophys. Res., 98, 18937.

Iyemori T. 1990, J. Geomagn. Geoelectr., 42, 1249.

Kamide Y., Baumjohann W., Gonzalez W. D., et al. 1998, J. Geophys. Res., 103, 17705.

Kilpua E. K. J., Olspert N., Grigoriev O., et al. 2015, Sol. Phys., 290, 965.

Kilpua E. K. J., Koskinen H. E. J., Pulkkinen T. I. 2017, Living Rev. Sol. Phys.

Kumar,S., Garg, S., Takur, P. S., Soni, S. L., & Tripathi, O. P. (2026). data.RendicontiLincei. ScienzeFisiche e Naturali, 37(1), 139–153.

Kumar S., Tripathi O. P., Sharma R., Verma P. L. 2023, Int. Astron. Astrophys. Res. J., 5, 65.

Kumar S., Verma P. L. 2023, J. Astrophys. Aerosp. Technol., 11, 4.

Kay C., et al. 2023, Space Weather, 21, e2022SW003647.

Mishra W. 2024, Mon. Not. R. Astron. Soc., 530, 3171.

Miteva R., et al. 2023, Atmospheres, 14, 1744.

Miteva R., Samwel S. W., Tkatchova S. 2023, Astronomy, 2(3), 165.

Nair M., et al. 2023, Space Weather, 21, e2023SW003514.

Richardson I. G., Cane H. V. 2012, Sol. Phys., 281, 187.

Rostoker G. 1972, Rev. Geophys., 10, 935.

Reyes P. I., Pinto V. A., & Moya P. S. 2021. Space Weather, 19, p.9.

Kumar S., et al. 2024, ApJ, **977, p.**57.

Shi T et al. 2024, Astrophys. J., 972, p.54.

Thakur et al. 2025, IJPAP, 64, p.304.

Tsurutani B. T., Gonzalez W. D. 1997, *Magnetospheric Current Systems*, Geophys. Monogr. Ser., 97, AGU.

Tsurutani B. T., Gonzalez W. D., Gonzalez A. L. C., et al. 2006, J. Atmos. Sol.-Terr. Phys., 69, 3.

Zhang J., Richardson I. G., Webb D. F., et al. 2007, J. Geophys. Res., 112, A10102.